arXiv:1611.06921v1 [cond-mat.stat-mech] 21 Nov 2016

Phase co-existence in bidimensional passive and active dumbbell systems

Leticia F. Cugliandolo,[1,2] Pasquale Digregorio,[3] Giuseppe Gonnella,[3] and Antonio Suma[4]

[1]*Sorbonne Universités, Université Pierre et Marie Curie - Paris VI, Laboratoire de Physique Théorique et Hautes Énergies, 4 Place Jussieu, 75252 Paris Cedex 05, France*
[2]*Kavli Institute for Theoretical Physics, University of California at Santa Barbara, CA 93106, USA*
[3]*Dipartimento di Fisica, Università degli Studi di Bari and INFN, Sezione di Bari, via Amendola 173, Bari, I-70126, Italy*
[4]*SISSA - Scuola Internazionale Superiore di Studi Avanzati, Via Bonomea 265, 34136 Trieste Italy*

(Received November 22, 2016)

We demonstrate that there is co-existence between hexatic order and liquid/gas phase over a finite interval of packing fractions in active repulsive dumbbell systems in two dimensions. In the passive limit this interval remains finite, similarly to what has been observed in bidimensional systems of hard and soft disks.

Bernard & Krauth argued that $2d$ melting of hard and soft repulsive disks occurs in two steps, with a continuous Berezinskii-Kosterlitz-Thouless transition between the solid and hexatic phases, and a first order transition between the hexatic and liquid phases, when density or packing fraction are decreased at constant temperature [1]. The hexatic phase has no positional order but quasi long-range orientational order, while the solid phase has quasi long-range positional and proper long-range orientational order. Liquid and quasi long-range orientationally ordered zones co-exist close to the liquid phase, within a narrow interval of packing fractions.

In recent years, interest in the behaviour of $2d$ (and also $3d$) macroscopic systems under continuous and homogeneous input of energy has been boosted by their connection with active matter [2–9]. This new type of matter can be realised in various ways. Systems of self-propelled particles constitute an important subclass, with natural examples such as suspensions of bacteria [10–12], and artificial ones made of Janus [13–15] or asymmetric granular [16] particles. In all these cases, the constituents consume internal or environmental energy and use it to displace. Very rich collective motion arises under these out of equilibrium conditions, and liquid, solid and segregated phases are observed [17–21]. Notably, segregation, also called motility induced phase separation, was claimed to exist *only at* large values of the activity. In this Letter we contest this belief and we show that the region of co-existence continuously links to the phase predicted by Bernard & Krauth in the passive limit.

We support our claim with a detailed numerical analysis of the dynamics of a bidimensional purely repulsive dumbbell system. The reason for choosing this model is that many natural swimmers have elongated shape, and a hard dimer is the simplest approximation of such anisotropy [22–24]. This geometry favours aggregation at intermediate densities and sufficiently strong activation [25–30]. In this limit the evolution of an initial homogeneous phase occurs by nucleation and growth of clusters [26] and the system phase separates. At the other extreme, for sufficiently low densities and not so strong activity, particles form only very small clusters that do not coalesce [28, 31, 32]. The results in this Letter complement these two extreme limits. In the absence of activity we confirm the scenario of Bernard, Kapfer & Krauth for hard and soft disks [1, 33, 34] using now a molecular system and we estimate the density interval for co-existence. We prove that this interval *continuously expands* towards the strong activity region where cluster aggregation had already been observed. Hence, there is no discontinuity between the passive and active regions in the phase diagram with phase separation. Figure 1 summarises this scenario that, we emphasise, is different from what has been stated in the literature so far, and that we justify with numerical evidence.

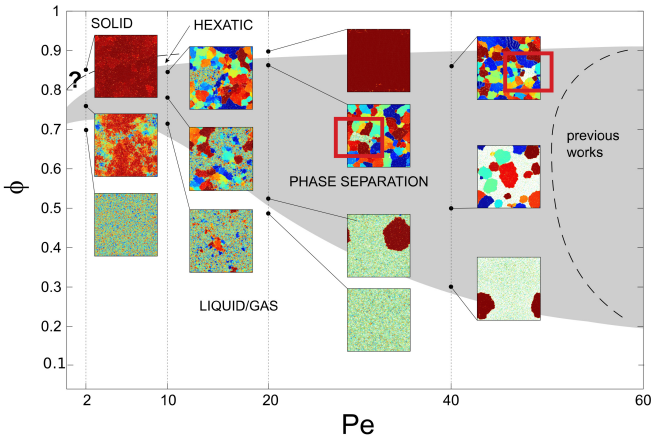

Figure 1. (Colour online.) The phase diagram and some representative local hexatic parameter maps. Note the red rectangular contours in the boxes at Pe $= 20$ and Pe $= 40$ that surround the disordered regions. The way in which the phase boundaries are determined is explained in the text and more details are given in the SM.

Event-driven algorithms have proven to be an efficient tool to equilibrate $2d$ interacting particle systems [35] and they have been used to give strong support to the two step phase transition scenario [1, 34]. We use, however, conventional molecular dynamics in order to simulate the out of equilibrium dynamics of active systems as realistically as possibly.

The dumbbell model consists of N diatomic molecules (dimers) with identical spherical head and tail centered at a fixed distance equal to their diameters, $\sigma_{\rm d}$. Any pair of dumbbells interact via a purely repulsive particular case of the so-called Mie potential, $U(r) = 4\epsilon[(r/\sigma)^{-2n} - (r/\sigma)^{-n}]$, trun-

cated at its minimum $r_c = 2^{1/n}\sigma$. r is the distance between the centers of any two disks. We set the characteristic length in U to $\sigma = 2^{-1/n}\sigma_{\rm d}$, so that $r_c = \sigma_{\rm d}$. Due to its softness, this potential allows small interpenetration of disks and thus disfavors the dense-phase formation. In order to get closer to hard core disks and be advantageous to existence of co-existence in the passive system [34] we used $n = 32$, a value that makes the overlap between particles less than $0.01\,\sigma_{\rm d}$. The evolution of the position $\mathbf{r}_i$ of the i-th bead is given by a Langevin equation,

$$m_{\rm d}\ddot{\mathbf{r}}_i = -\gamma_{\rm d}\dot{\mathbf{r}}_i - \boldsymbol{\nabla}_i U + \boldsymbol{F}_{\rm act} + \sqrt{2k_BT\gamma_{\rm d}}\,\boldsymbol{\eta}_i(t), \quad (1)$$

where $\gamma_{\rm d}$ is the friction coefficient, $\boldsymbol{\nabla}_i = \partial_{\mathbf{r}_i}$, T is the temperature of the thermal bath, $m_{\rm d}$ is the mass of a bead, $\boldsymbol{F}_{\rm act}$ is a tail-head-directed active force with constant magnitude $F_{\rm act}$, and $\boldsymbol{\eta}_i(t)$ is an uncorrelated Gaussian noise with zero mean and unit variance. An additional force, not written explicitly in Eq. (1), takes into account the holonomic constraint that fixes the dumbbell head-tail distance. We set the parameters to be in the over-damped limit [36]. The dimensionless control parameters are the area fraction covered by the active particles, $\phi = N\pi\sigma_{\rm d}^2/(2A)$, where $A = L^2$ is the area of the simulation domain, and the Péclet number, $\mathrm{Pe} = 2F_{\rm act}\sigma_{\rm d}/(k_BT)$. All data were obtained using a simulation box with linear size $L \approx 500\,\sigma$ and periodic boundary conditions. Each run took, typically, an evolution time of the order of 5×10^5 simulation time units (MDs [36] that we do not write explicitly henceforth). We performed some tests in systems with $L \approx 1500\,\sigma$ run for longer and we found no notable differences with the results shown. More details on the algorithm and running-times are given in the Supplemental Material (SM).

We quantify our assertions with the measurement of two observables: the *local densities* ϕ_j measured in two ways explained in the SM with equivalent results, and the *local hexatic parameter* evaluated as

$$\psi_{6j} = \frac{1}{N_{\rm nn}^j}\sum_{k=1}^{N_{\rm nn}^j} e^{6{\rm i}\theta_{jk}}, \quad (2)$$

where the sum runs over the $N_{\rm nn}^j$ nearest neighbours of the bead j and θ_{jk} is the angle between the segment that connects j with its neighbour k and the x axis. The nearest neighbours are found using the Voronoi tessellation with the algorithm in [37] that takes into account the periodic boundary conditions. For beads regularly placed on the vertices of a triangular lattice, each site has six nearest-neighbours, $\theta_{jk} = 2k\pi/6$, and $\psi_{6j} = 1$. We also consider the modulus of the average per particle and the average per particle of the modulus,

$$2N\,\psi_6 \equiv \left|\sum_{j=1}^{N}\psi_{6j}\right|, \qquad 2N\,\Gamma_6 \equiv \sum_{j=1}^{N}|\psi_{6j}|\,, \quad (3)$$

respectively. In order to visualise the local values of ψ_{6j} we attribute a colour code as proposed in [1]: first, the complex local values ψ_{6j} are projected onto the direction of their space average and normalised, next, each bead is coloured according to this projection. Zones with orientational order have uniform colour, whatever it is.

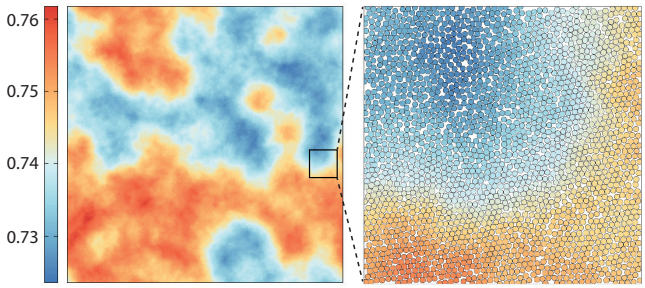

Figure 2. (Color online.) Passive system with $\phi = 0.74$ in equilibrium. Left: the density plot constructed by averaging the local density over a region with radius equal to $20\,\sigma$. Right: a zoom over the region within the black square in the left plot showing the individual dumbbells close to the interface between a region with hexatic order (lower right) and a disordered sector (upper left). The color code is the same as in the left panel. The local hexatic map for this configuration is shown in the central upper panel in Fig. 3.

We start by analysing the passive system. We use three kinds of initial states with the desired global packing fraction ϕ: random configurations with positions and orientations uniformly distributed, striped initial states with an ordered close-packed slab embedded in vacuum, and a hexatic-ordered state (for more details, see Sec. S1 in the SM). In all cases we present data that have evolved during sufficiently long time to ensure that the initial state is forgotten and equilibration is reached. In the SM we exemplify the transient dynamics.

For $\phi < 0.730$ any initial state with phase separation quickly melts. Hence, any initial configuration eventually evolves as a liquid. This is confirmed, for instance, by the fact that translational and hexatic correlation functions decay exponentially with distance. Above $\phi \approx 0.756$ initial states with hexatic order remain ordered and the corresponding correlation decays very slowly. (Figure S3 shows the hexatic correlation functions for different packing fractions and, for $\phi > 0.756$, it appears constant in this scale.) In between there is a regime with co-existence, as we now prove.

The first evidence for co-existence is given in Fig. 2 where we show the local density plot in equilibrium at the global packing fraction $\phi = 0.74$ (left panel), with a zoom close to an interface between dense and sparse regions (right panel). The individual dumbbells are painted with the color code of the local density at their position. The hexatic order in the region with high density and the lack of orientational order in the sparse region are clear in the zoom.

Further evidence for co-existence at this and other global densities is given in the upper panels in Fig. 3 where we show the local hexatic parameter on three equilibrium snapshots at $\phi = 0.734,\ 0.740,\ 0.750$. These configurations are chosen at the long-time limit of the evolution of random initial states.

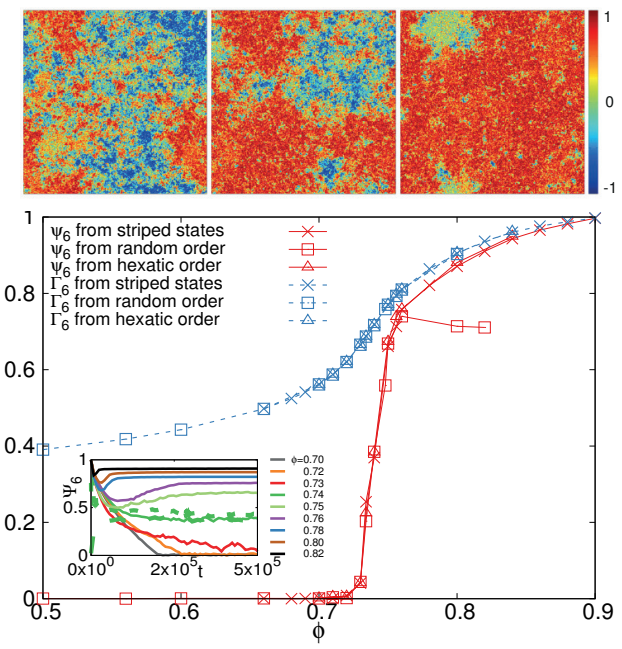

Figure 3. (Color online.) Passive system. Above: the local hexatic parameter, ψ_{6j}, in equilibrium configurations at $\phi = 0.734,\ 0.740,\ 0.750$ from left to right. Below: the modulus of the averaged local hexatic order parameter, ψ_6, and the average of the modulus of the local hexatic order parameter, Γ_6, as functions of ϕ. The data correspond to asymptotic states reached from random, hexatic-ordered and striped initial conditions, as indicated in the key. In the inset we plot the time evolution of ψ_6 from striped initial conditions at various densities with different solid lines. We also display the evolution at $\phi = 0.74$ from random and hexatic-ordered initial states with dashed and dotted lines, respectively. For transient and asymptotic snapshots see Fig. S2.

The regions with local hexatic order are also regions of local high density and, conversely, in the sparse regions the dumbbells do not have orientational order (see Fig. S4 in the SM where the corresponding density plots as the ones in Fig. 2 and histograms of the local densities are shown). In the plot below we display the asymptotic ψ_6 and Γ_6 defined in Eq. (3) against ϕ for the three kinds of initial conditions. The data have been averaged over all particles in the sample and over the last ten configurations (sampled every $\sim 10^4$). The results confirm that the departing state is forgotten as the curves coincide within numerical accuracy. Only one curve is an exception, the one for ψ_6 and random initial configuration at $\phi \gtrsim 0.780$ that still has to undergo a coarsening process to orient the clusters in the same direction, see Fig. S6 in the SM. All curves increase with ϕ indicating that the proportion of regions with hexatic order with respect to the disordered ones grows with ϕ. The curve Γ_6 against ϕ is continuous and smooth while the one for ψ_6 although also continuous, shows a very steep increase starting at the smallest density at which co-existence appears. In the inset we show the time-dependence of ψ_6 at densities in the interval $[0.7, 0.82]$ in steps of 0.02 and the case $\phi = 0.730$ close to the border. All curves approach an asymptote, that vanishes for $\phi < 0.730$, but detaches from zero and grows with ϕ for $\phi > 0.730$. For $\phi = 0.740$ we follow with different line types the evolution of the three kinds of initial states to prove that they all approach the same asymptote. Figure S2 illustrates the evolution of the local ψ_{6j} for these three initial conditions. The last one in the series is at a time at which the (green) curves in Fig. 3 have reached the plateau, that is to say, after the initial state has been forgotten.

Turning these arguments into a quantitative analysis, we find co-existence in the passive system in the interval $\phi \in [0.730,\ 0.756]$, approximately, justifying the extent of the grey region on top of the Pe = 0 axis in Fig. 1.

We now switch on activity. We first focus on a density that lies within the interval where the system shows co-existence in its passive limit, $\phi = 0.734$. In Fig. 4 we display the local hexatic order parameter of three instantaneous configurations obtained from the evolution at Pe = 10 of different initial conditions. The snapshots above are for an initial configuration with co-existence between a dense region with a rough horizontal form and a sparse region around it. Below are the snapshots for an initial stationary state at Pe = 40 where the system is strongly segregated. The times are given in the caption with a convention such that the initial state is at $t = 0$. In the first case the system breaks the horizontal dense region and it later recreates dense clusters of approximately round form. These clusters turn independently of one another and they consequently have different (time-dependent) local hexatic order. Movie M1 illustrates the aforementioned dynamics

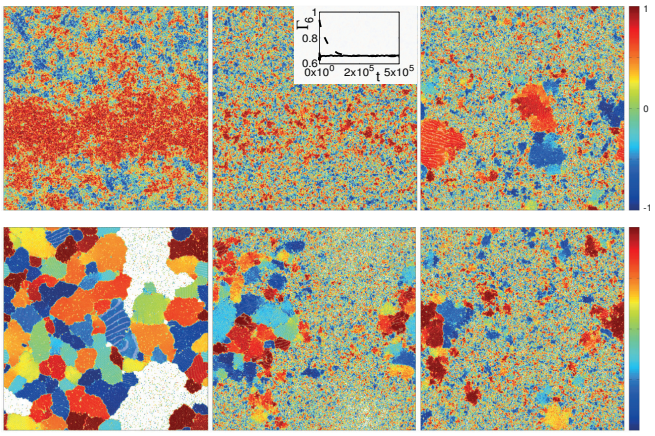

Figure 4. (Colour online.) Time evolution at Pe = 10 and $\phi = 0.734$. The initial states for the sequences above and below are the first snapshots in each row and correspond to a phase separated configuration at Pe = 0 evolved from a configuration with a striped-state of dumbbells (see Fig. S2 and its discussion in the SM) and the steady state at Pe = 40, respectively. The white zones are almost empty and the system is in its gaseous phase in them (cfr. Figs. S10 (d) in the SM where the evolution of a system at Pe = 40 and a lower packing fraction, $\phi = 0.40$, shows similar though larger gaseous regions). The times at which the subsequent snapshots are taken are $t = 2.5 \times 10^2,\ 8.6 \times 10^5$ above and $t = 10^5,\ 6 \times 10^5$ below. As an inset in the middle upper image we include the time-dependence of the parameter Γ_6 for the two runs.

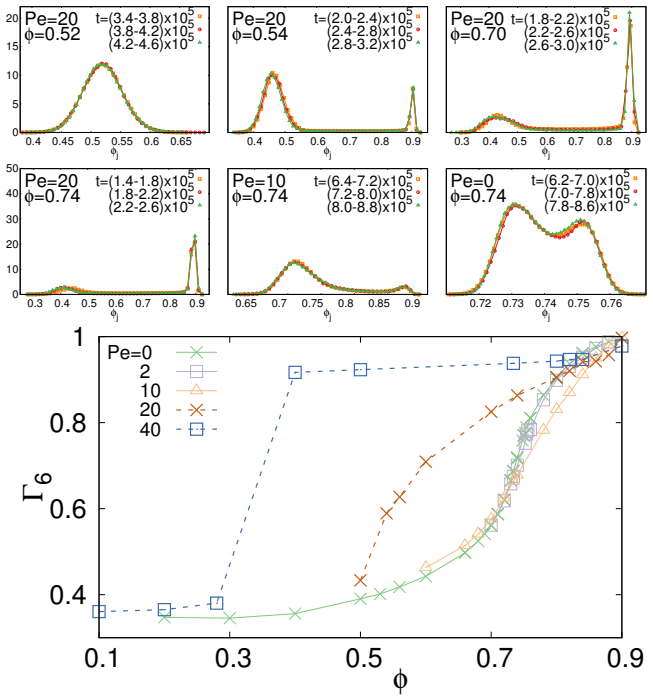

Figure 5. (Colour online.) Distributions of local densities at $\phi = 0.52,\ 0.54,\ 0.7$ and fixed Pe= 20 (from left to right, first row) and Pe $= 20,\ 10,\ 0$ and $\phi = 0.74$ (from left to right, second row). The initial configurations for the first line are random, for the second line are the equilibrium configurations for the passive system at the given total density. The various curves correspond to data sampled over different time intervals made explicit in the keys. The third plot shows Γ_6 as a function of ϕ for several Pe, given in the key.

at $\phi = 0.74$, with more details on the cluster formation. In the second case, dumbbells are progressively evaporated from the large and dense clusters until less packed and smaller ones attain a stable size. Simultaneously, the regions in between the dense clusters reach the target density of the sparse phase. The subsequent dynamics are the same as for the steady state reached in the upper series of snapshots. In the inset in the middle upper image we show the time-dependence of the parameter Γ_6 for the two runs, and we verify that they reach the same asymptote after a transient. Therefore, independently of the initial conditions, the dynamics at $\phi = 0.734$ and Pe = 10 approach a stationary limit with co-existence. The same occurs for all Pe at this ϕ, even the very small ones (supplementary information on the Pe = 2 case is given in Fig. S7).

Having established that a small amount of activity does not destroy the co-existence present in the passive system at $\phi = 0.734$, we need to find out what happens at other packing fractions and, more precisely, we ought to determine how the activity affects the limits of co-existence. To this end, we set up a more quantitative analysis of the steady state configurations obtained by sweeping the parameters ϕ and Pe.

With the data for the coarse-grained local density at different pairs (ϕ, Pe) we built the probability distribution functions shown in Fig. 5. In the first row Pe = 20 and $\phi = 0.52,\ 0.54,\ 0.7$ (Fig. S8 shows the dynamics at the intermediate density). The first panel presents a static symmetric distribution around the global packing fraction that is in the liquid phase close to the boundary. The second panel shows the emergence of a second peak at a higher density, $\phi_j \simeq 0.9$, while the weight on lower density has displaced to a lower value of ϕ_j. The third panel confirms the presence of the peak at $\phi_j \simeq 0.9$, the height of which has notably increased. Consequently, the weight on smaller local densities decreased and has displaced towards a slightly smaller value. The appearance of the second peak is our criterium to draw the upper boundary of the homogeneous phase and the entrance into the phase separated region of the phase diagram at fixed Pe. At higher packing fractions the position of the second peak does not vary but its height increases at the expense of the one of the first peak. The upper boundary of the phase segregated region is naturally determined by the disappearance of the low density peak (a comparison between configurations below and above the upper phase boundary of the segregated region is made in Fig. S9).

The second row in Fig. 5 displays the Pe-dependence of the local density plots at $\phi = 0.74$, well into the co-existence interval in the passive limit. This analysis confirms continuity between the steady states in the passive and active cases. The Pe numbers are 20 (left), 10 (center) and 0 (right) moving from right to left in the phase diagram. The position of the high density peak moves towards larger ϕ_j for increasing Pe, indicating that the dense regions become more compact, and accordingly the loose regions become more void, as Pe increases at fixed global packing fraction. This fact indicates that segregation is more effective at higher Pe.

Alternatively to the study of the local density, the hexatic order can also be used to analyze the phase diagram. At Pe = 0 we could use the steep increase of ψ_6 (around $\phi = 0.734$, see Fig. 3) to locate the phase boundary from liquid to phase separated phases. In fact, the passive system selects a single global value of ψ_6 everywhere, and this quantity is well behaved since it does not have large fluctuations around its full sample average. At finite Pe, instead, there are clusters with rather different values of ψ_6. For this reason, it is more convenient to use, instead, Γ_6 as an alternative to the local density distributions, to study this boundary in the active system. In the lower panel in Fig. 3 we show Γ_6 as a function of ϕ for various Pe values. There is little dependence on Pe for, say, Pe $\lesssim 10$, while for larger values the shoulder moves towards smaller densities, signalling that the phase boundary becomes one between gas (very low ϕ) and segregated phases at higher Pe (see also Fig. S8).

Movies M2-M4 complement this survey with emphasis on the coarsening at Pe = 2, 10, 20, see the SM.

Putting these results together we draw the phase diagram in Fig. 1. The figure also includes, as illustrations, some configurations at parameter values close to the limits of co-existence that clearly show liquid, phase separated and hexatic order. Let us recap the main features of the phase diagram. The lower boundary of the co-existence region decreases with increasing Pe since large activity favors the for-

mation of high density clusters and therefore co-existence. Furthermore, co-existence is allowed at higher global packing fractions. This is because the regions with hexatic order become denser and leave more free space for the liquid phase under higher Pe [38]. We conclude that we do not see any discontinuity between the behaviour of the system at Pe = 0 and Pe > 0 at the densities at which there is phase co-existence in the passive limit.

As in a conventional liquid-vapor transition, it is very hard to establish where the first-order transition lies with high precision. It would be desirable to complement our analysis with a thermodynamic study of the phase transitions. The double transition scenario proposed in [1] for the $2d$ passive hard disk problem was confirmed by the finite-size analysis of the equation of state, or packing-fraction dependence of the pressure in the NVT ensemble [1, 33]. In contrast, the existence of an equation of state in generic active matter remains open. Indeed, the difficulty to precisely define a pressure with the properties of a state variable in active systems was underlined in a number of papers, see e.g. [29, 39, 40]. The results here presented should further stimulate the search for a consistent definition of pressure for (molecular) active matter.

Simulations have been performed on IBM Nextscale GALILEO at CINECA (Project INF16-fieldturb) under CINECA-INFN agreement and at Bari ReCaS e-Infrastructure funded by MIUR through the program PON Research and Competitiveness 2007-2013 Call 254 Action I. GG acknowledges MIUR for funding (PRIN 2012NNRKAF). This research was supported in part by the National Science Foundation under Grant No. NSF PHY-1125915. LFC is a member of the Institut Universitaire de France. We thank R. Golestanian for early discussions.

[1] E. Bernard and W. Krauth, Phys. Rev. Lett. **107**, 155704 (2011).
[2] J. Toner, Y. Tu, and S. Ramaswamy, Ann. of Phys. **318**, 170 (2005).
[3] D. A. Fletcher and P. L. Geissler, Ann. Rev. Phys. Chem. **60**, 469 (2009).
[4] P. Romanczuk, M. Bär, W. Ebeling, B. Lindner, and L. Schimansky-Geier, Eur. Phys. J. Special Topics **202**, 1 (2012).
[5] T. Vicsek and A. Zafeiris, Phys. Rep. **517**, 71 (2012).
[6] M. E. Cates, Rep. Prog. Phys. **75**, 042601 (2012).
[7] M. C. Marchetti, J. F. Joanny, S. Ramaswamy, T. B. Liverpool, J. Prost, M. Rao, and R. A. Simha, Rev. Mod. Phys. **85**, 1143 (2013).
[8] G. de Magistris and D. Marenduzzo, Physica A **418**, 65 (2015).
[9] J. Elgeti, R. Winkler, and G. Gompper, Rep. Prog. Phys. **78**, 056601 (2015), 1412.2692.
[10] X.-L. Wu and A. Libchaber, Phys. Rev. Lett. **84**, 3017 (2000).
[11] C. Dombrowski, L. Cisneros, S. Chatkaew, R. Goldstein, and J. Kessler, Phys. Rev. Lett. **93**, 098103 (2004).
[12] A. Rabani, G. Ariel, and A. Be'er, PLOS ONE **8**, 1 (2013).
[13] W. F. Paxton, K. C. Kistler, C. C. Olmeda, A. Sen, S. K. S. Angelo, Y. Cao, T. E. Mallouk, P. E. Lammert, and V. H. Crespi, J. Am. Chem. Soc. **126**, 13424 (2004).
[14] I. Buttinoni, J. Bialké, F. Kümmel, H. Löwen, C. Bechinger, and T. Speck, Phys. Rev. Lett. **110**, 238301 (2013).
[15] F. Ginot, I. Theurkauff, D. Levis, C. Ybert, L. Bocquet, L. Berthier, and C. Cottin-Bizonne, Phys. Rev. X **5**, 011004 (2015).
[16] K.-D. N. T. Lam, M. Schindler, and O. Dauchot, New J. Phys. **17**, 113056 (2015).
[17] J. Tailleur and M. E. Cates, Phys. Rev. Lett. **100**, 218103 (2008).
[18] Y. Fily and M. C. Marchetti, Phys. Rev. Lett. **108**, 235702 (2012).
[19] J. Stenhammar, A. Tiribocchi, R. J. Allen, D. Marenduzzo, and M. E. Cates, Phys. Rev. Lett. **111**, 145702 (2013).
[20] G. S. Redner, M. F. Hagan, and A. Baskaran, Phys. Rev. Lett. **110**, 055701 (2013).
[21] A. Wysocki, R. G. Winkler, and G. Gompper, EPL **105**, 48004 (2014).
[22] K. W. Wojciechowski, D. Frenkel, and A. C. Brańka, Phys. Rev. Lett. **66**, 3168 (1991).
[23] K. W. Wojciechowski, A. C. Brańka, and D. Frenkel, Physica A **196**, 519 (1993).
[24] C. Valeriani, M. Li, J. Novosel, J. Arlt, and D. Marenduzzo, Soft Matter **7**, 5228 (2011).
[25] F. Peruani, A. Deutsch, and M. Bär, Phys. Rev. E **74**, 030904(R) (2006).
[26] G. Gonnella, A. Lamura, and A. Suma, Int. J. Mod. Phys. C **25**, 1441004 (2014).
[27] A. Suma, D. Marenduzzo, G. Gonnella, and E. Orlandini, EPL **108**, 56004 (2014).
[28] L. F. Cugliandolo, G. Gonnella, and A. Suma, Phys. Rev. E **91**, 062124 (2015).
[29] M. Joyeux and E. Bertin, Phys. Rev. E **93**, 032605 (2016).
[30] G. Gonnella, D. Marenduzzo, A. Suma, and A. Tiribocchi, Comptes Rendus Physique **16**, 316 (2015).
[31] A. Suma, G. Gonnella, G. Laghezza, A. Lamura, A. Mossa, and L. F. Cugliandolo, Phys. Rev. E **90**, 052130 (2014).
[32] A. Suma, L. F. Cugliandolo, and G. Gonnella, Chaos & solitons **81**, 556 (2015).
[33] M. Engel, J. A. Anderson, S. C. Glotzer, M. Isobe, E. P. Bernard, and W. Krauth, Phys. Rev. E **87**, 042134 (2013).
[34] S. Kapfer and W. Krauth, Phys. Rev. Lett. **114**, 035702 (2015).
[35] E. Bernard, W. Krauth, and D. B. Wilson, Phys. Rev. E **80**, 056704 (2009).
[36] All physical quantities are expressed in reduced units [**?**] of the sphere's mass $m_{\rm d}$, diameter $\sigma_{\rm d}$ and potential energy ϵ. The time unit is the standard Lennard-Jones time $\tau_{LJ} = \sigma_{\rm d}(m_{\rm d}/\epsilon)^{1/2}$. Other important simulation parameters, in reduced units, are $\gamma_{\rm d} = 10$, $k_BT = 0.05$ and we set $k_B = 1$.
[37] C. H. Rycroft, Chaos **19**, 041111 (2009).
[38] We did not consider here the transition between the hexatic and crystalline phases (dashed line in Fig. 1) that has been studied, for a colloidal active system, in [**?**].
[39] A. P. Solon, J. Stenhammar, Y. Kafri, M. E. Cates, and J. Tailleur, Phys. Rev. Lett. **114**, 198301 (2015).
[40] A. Patch, D. Yllanes, and M. C. Marchetti, "Kinetics of motility-induded phase separation and swim pressure," (2016), arXiv:1610.01139.
[41] H. C. Andersen, J. Comp. Phys. **52**, 24 (1983).

Supplemental Material for "Phase co-exitence in bidimensional passive and active dumbbell systems"

S1. METHODS

Integration of the equation of motions

The integrator is a velocity Verlet algorithm that solves Newton's equations of motion, plus additional force terms for the Langevin-type thermostat. The bonds are kept rigid by using the RATTLE scheme [41]. The time-step choice is related to the force exerted during the simulation, and we adapted it to enforce the numerical stability. For systems at Pe ≤ 10 a time-step of 0.008 is sufficient. For larger values of Pe we needed to reduce it to 0.002. One simulation unit (equal to $1\,\tau_{LJ}$, i.e. one Lennard-Jones time-unit, $\tau_{LJ} \equiv \sigma_{\rm d}(m_{\rm d}/\epsilon)^{1/2}$) corresponds to 125 integration steps in the case of a unit time-step of 0.008 and 500 integration steps in the case of a unit time-step of 0.002.

We used the open source software Large-scale Atomic/Molecular Massively Parallel Simulator (LAMMPS), available at `github.com/lammps`, to efficiently parallelize the numerical computation.

In addition to the results presented in this manuscript, in the passive case, we also studied the behavior of the system using the Weeks-Chandler-Andersen (WCA) potential between the spheres, that corresponds to $n = 6$ in the potential $U(r)$ defined in the main text and a truncation at $r_c = 2^{1/6}\,\sigma_d$. The dumbbells were still considered rigid with a distance σ_d between the centers of their beads. With this choice, we found very similar results to the ones shown in this work for $n = 32$, but with a consistently smaller coexistence region due to the softness of the potential that disfavors the hexatic ordering.

On average each simulation lasting 5×10^5 Molecular Dynamics units was run on 16 processors for a total of 100 hours for each cpu. All runs in the coexistence region where run for a larger amount of time, around 3×10^6, in order to check stationarity.

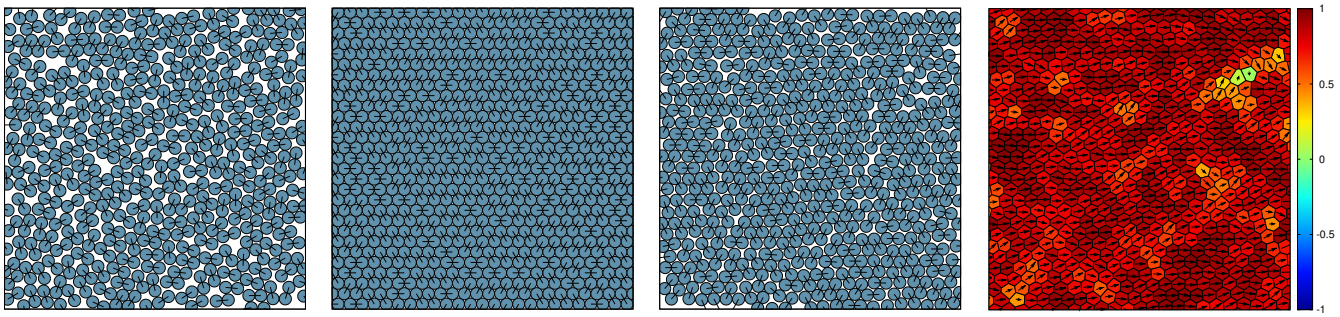

(a) (b) (c) (d)

Figure S1. (a) Random configuration with $\phi = 0.70$. (b) Closed-packed configuration with $\phi = 0.91$ and randomly oriented dumbbells. (c) Hexatically-ordered configuration with $\phi = 0.80$ (see the text for details on how it is built). The local hexatic parameter is about the same, except for weak fluctuations, to its average over the whole system, as shown in (d), where the Voronoi cells, with an internal arrow with the direction of the local vector ψ_{6j}, are shown.

Construction of the initial conditions

In all our simulations we used three kinds of starting configuration that we call 'striped', 'random' and 'hexatic-ordered' in the text. We explain how we obtained these initial states below.

Random initial condition. The dumbbells are placed at random positions, with random orientations, in continuous space. At large ϕ this construction yields, very likely, states with overlapping dumbbells. For the parameters used, the maximum overlap accepted is $0.75\,\sigma$. Consequently, these configurations can have a very high energy. The excess energy is then released by letting the system equilibrate with a softer Lennard-Jones potential and a smaller time-step equal to 0.001. After this procedure, convenient starting configurations as the one shown in Fig. S1 (a) are found and then used in the simulation with the purely repulsive potential defined in the main text.

Striped states. The dumbbells are placed in a closed-packing triangular lattice with zero average global orientation, leaving an empty slab in order to have the right density, as depicted in Fig. S2, first panel. The part covered by the dumbbells is sketched in Fig. S1 (b). Configurations like that in Fig. S2 are constructed by placing the dumbbells in sequence starting from the bottom-left end, say, until their number satisfies the required global density. The orientational order in the configuration is then randomised with Monte Carlo moves that take two adjacent dumbbells and exchange their bonds. In this way, the molecules are still placed in a crystal configuration but their directions are completely random.

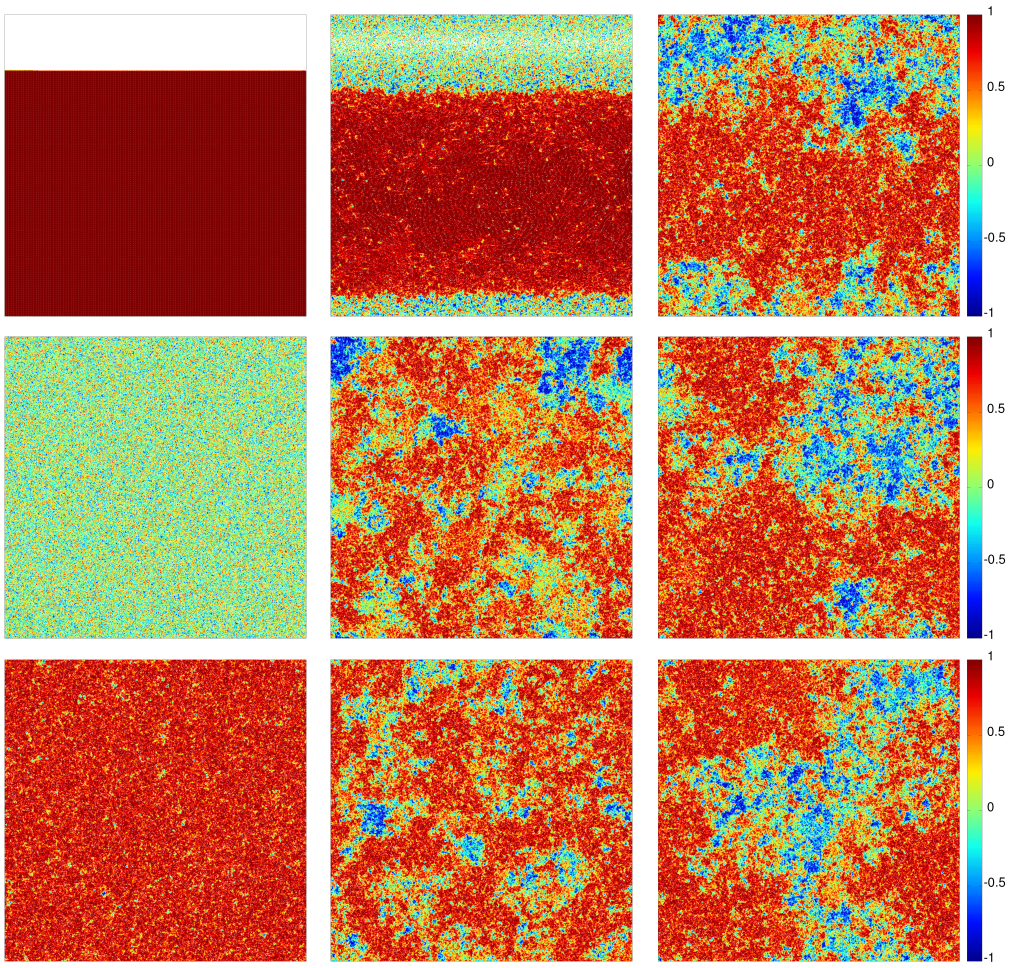

Figure S2. **Evolution of the passive system in the co-existence region of the phase diagram. Loss of memory of the initial configurations.** Local hexatic order grey-scale (colour online) map according to the scale defined on the right bars. The packing fraction is $\phi = 0.74$. The three rows correspond to striped, random and hexatic-ordered starting configurations shown in the first panel on each row. The two subsequent panels on the three rows are taken at later times, given explicitly in the text.

Initial configuration with hexatic order. We built such a configuration at the desired density following the steps now listed. First, we took an equilibrated crystalline configuration with hexatic order like the one depicted in Fig. S1 (c)-(d), with packing fraction just above the coexistence region at $\mathrm{Pe} = 0$. This is obtained by equilibrating the system starting from a striped configuration with this packing fraction, see the sequence of snapshots in Fig S5, last row. We then expanded (or contracted) the configuration by multiplying the coordinates with a convenient factor α, thus obtaining a rescaled system. Accordingly, the system size is now rescaled to αL, which is at most $20\,\sigma$ larger (or smaller) than the original one, depending on the chosen density that we want to simulate. Finally we applied a short equilibration run with a smaller time-step equal to 0.001 to obtain the starting configuration. For the densities considered, the rescaling is small enough to preserve the initial hexatic ordering without blowing up the simulation.

Measurement of the local density

We compute the local density in two ways.

With the first method, for each bead, we first estimate the local density as the ratio between its surface and the area of its Voronoi region. We next coarse-grain this value by averaging the single-bead densities over a disk with radius $10 - 20\,\sigma$. Each Voronoi region is then painted with the colour that corresponds to its coarse-grained local density value, denser in red, looser in blue.

With the second method, we construct a square grid on the simulation box. For each point in the grid we calculate a coarse grained local density over a circle of given radius. We finally assign this density value to the grid point.

S2. EQUILIBRIUM AT COEXISTENCE IN THE PASSIVE CASE, PE = 0

In this Section we illustrate the transient dynamics and we give additional details on the steady state reached at long times by the passive system.

We first focus on the coexistence region and we show that the steady states are independent of the choice of the initial configuration. In Fig. S2 we show the local hexatic parameter grey (colour online) map of the system evolved from three different initial conditions, all with global packing fraction $\phi = 0.74$, plotted in the first panel of each row. These are a striped state with a sharp interface between closed-packed and empty regions in the first row, a state with neither positional nor orientational order in the second row, and a configuration with hexatic order in the third row constructed in the way explained in the previous Section. We then let these states evolve during a very long time and we show typical configurations observed later in the second and third panels on each row. These maps are taken at $t = 4 \times 10^4$ and 8.5×10^5 in the first row, $t = 4 \times 10^4$ and 1.3×10^6 in the second row, and $t = 4 \times 10^4$ and 1.2×10^6 in the third one. At the last time of each case the system is in stationary conditions as it can be seen in Fig. 3 in the main text from the common value reached by ψ_6. It is clear from the last snapshots on each row that the initial configurations have been either totally or partially forgotten and that the system approaches a situation with co-existence between the liquid phase and the phase with hexatic order. Similar behaviour is seen at $\phi = 0.734$ and $\phi = 0.75$, two packing fractions that are close to the lower and the upper limits of the co-existence region in the phase diagram, though still within it.

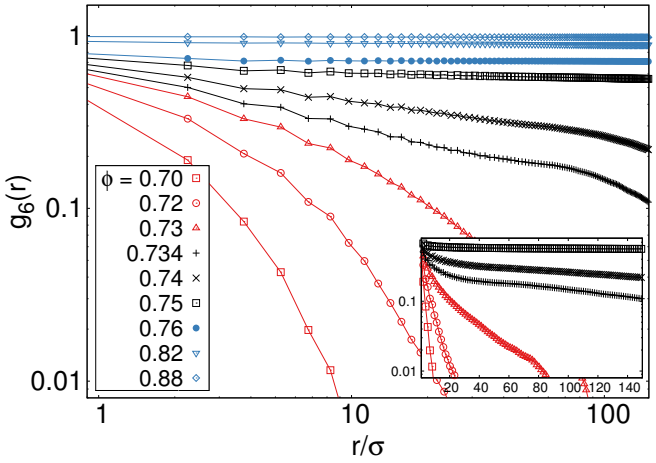

Figure S3. **Hexatic correlation functions in the steady state** for different packing fractions.

Figure S3 displays the hexatic order correlation function

$$g_6(r) = \langle \psi_{6j}^* \psi_{6k} \rangle \big|_{|\vec{r}_j - \vec{r}_k| = r} \, / \langle |\psi_{6j}|^2 \rangle \tag{S1}$$

at different packing fractions. The average is taken over different configurations at different times in the stationary regime. In the main panel the data are plotted in double logarithmic scale, that highlights the fact that the decay is power-law (with an exponential cut-off at distances comparable with the typical size of hexatically ordered regions) for parameters in the co-existence region in the phase diagram. In the inset we present the same data in linear-log scale to show that the decay is exponential in the liquid phase (cases $\phi < 0.73$ in the figure). Finally, the set of data for high values of the packing fraction, $\phi > 0.76$, decay so

slowly that do not decay beyond a finite value. Note that in the proper hexatic phase bond-orientation correlation functions are expected to decay algebraically. Nevertheless, it would be necessary to use much larger system sizes to see this power law.

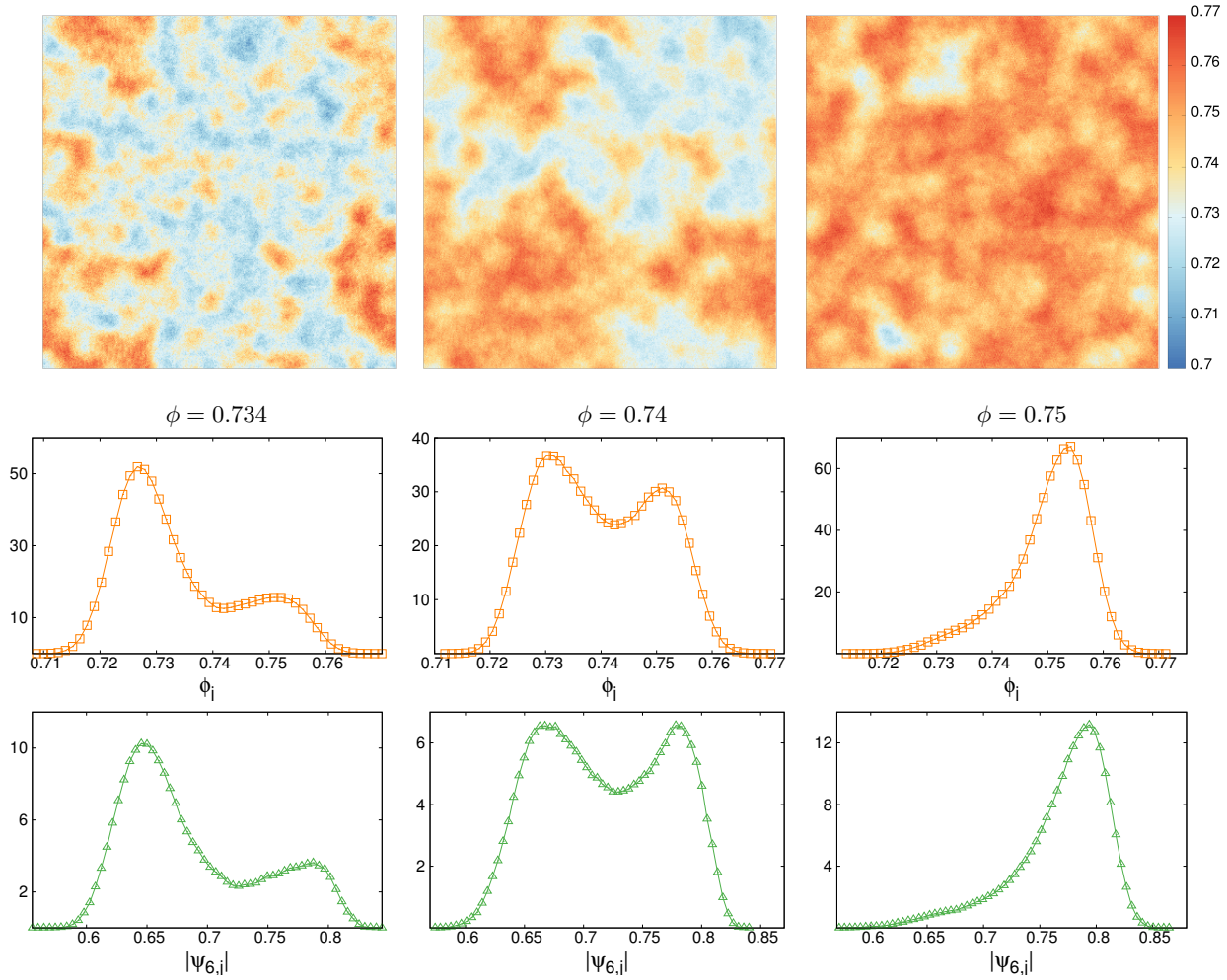

Figure S4. **Stationary state of the passive system in the co-existence region of the phase diagram, cfr. Fig. 3 in the main text**. The local density contour plot (first row), the probability distribution function of the local density (middle row) and the probability distribution function of the local hexatic modulus (third row) in the stationary limit of three passive systems with $\phi = 0.734$ (first column), $\phi = 0.74$ (second column) and $\phi = 0.75$ (third column).

Figure S4 gives support to the results in Fig. 3 and its discussion in the main text. We display here the local density contour plot in the same stationary configuration of the passive system in Fig. 3 (above), the probability distribution of the local density (middle) and the probability distribution of the local hexatic modulus (below) in the steady state with packing fractions $\phi = 0.734$ (first column), $\phi = 0.74$ (second column) and $\phi = 0.75$ (third column). The local density contour plots show a very similar pattern to the local hexatic parameter contour plots of Fig. 3 in the main text: the spatial distribution of the regions with high and low local density and high and low local hexatic parameter are highly correlated. The double peaked structure of the local density distribution functions (second row in the figure) in the cases $\phi = 0.734$ (first panel) and $\phi = 0.74$ (second panel) give more quantitative evidence for the fact that these packing fractions are in the co-existence region of the phase diagram. Instead, for the higher packing fraction $\phi = 0.75$ (third panel) the almost complete disappearance of the peaks at low local density and weak value of the local hexatic modulus, concomitant with the transfer of weight towards the peaks at large values of these two observables, signals that the system is close to the boundary with the single phase region of the phase diagram. Using lower global density, a value is reached below which the peak at higher density disappears signalling the passage to the liquid phase.

In Fig. S5 we compare the dynamics and steady states at three packing fractions: one in the liquid region of the phase diagram close to the lower limit of co-existence, $\phi = 0.72$ in the first row, another one within the region of the phase diagram with

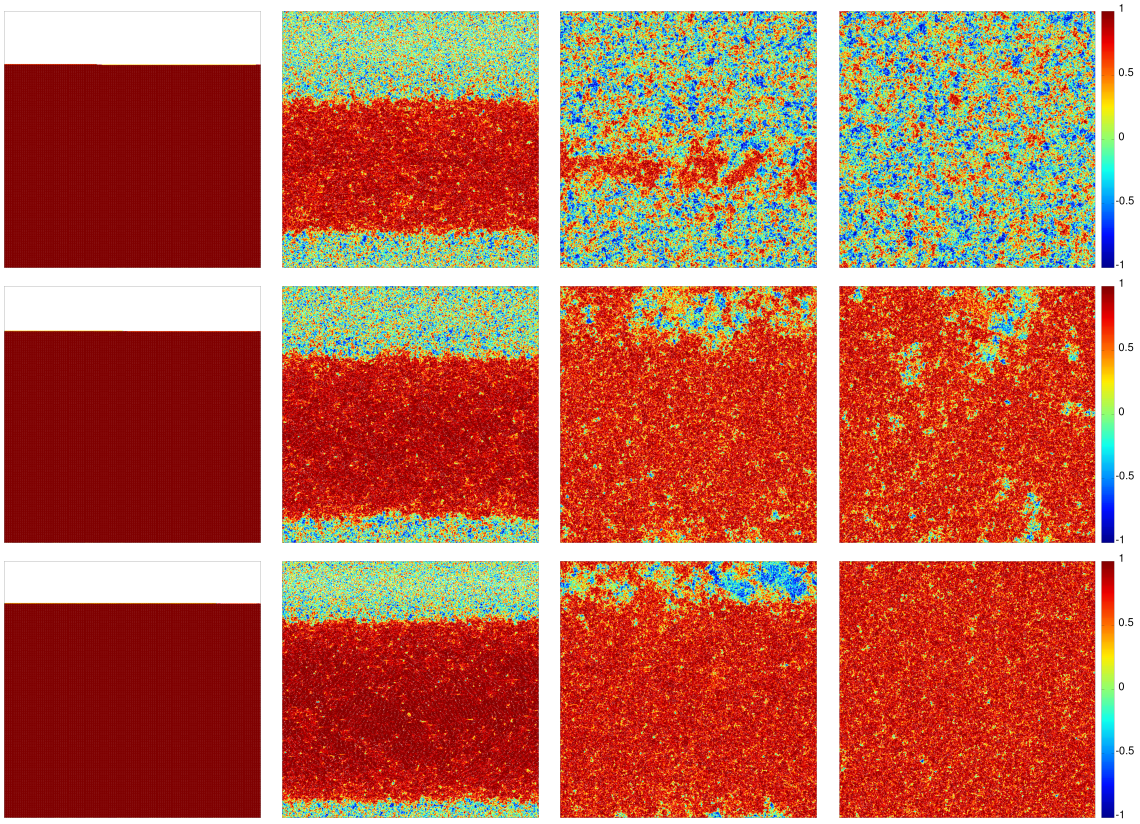

Figure S5. **Comparison between the evolution of the passive system at different packing fractions.** The packing fractions are $\phi = 0.72,\ 0.75,\ 0.76$ from top to bottom and the initial state is a striped configuration in the three cases. See the text for more details on this figure, and in particular the times at which the grey-scale (colour online) maps are measured.

co-existence but close to its upper limit, $\phi = 0.75$ in the second row, and one in the region with homogeneous hexatic order at $\phi = 0.76$ in the third row. The initial states are shown in the first panel in each row and they are always striped states with a neat separation between closed-packed and empty-space regions. The times at which the snapshots are taken are $t = 0,\ 8 \times 10^4$, 2.4×10^5 and 5.1×10^5 for $\phi = 0.73$, $t = 0,\ 4 \times 10^4,\ 3.2 \times 10^5$ and 7.7×10^5 for $\phi = 0.75$ and $t = 0,\ 4 \times 10^4,\ 1.8 \times 10^5$ and 5.7×10^5 for $\phi = 0.76$. It is quite clear from the last snapshots on the three rows that the stationary states attained are quite

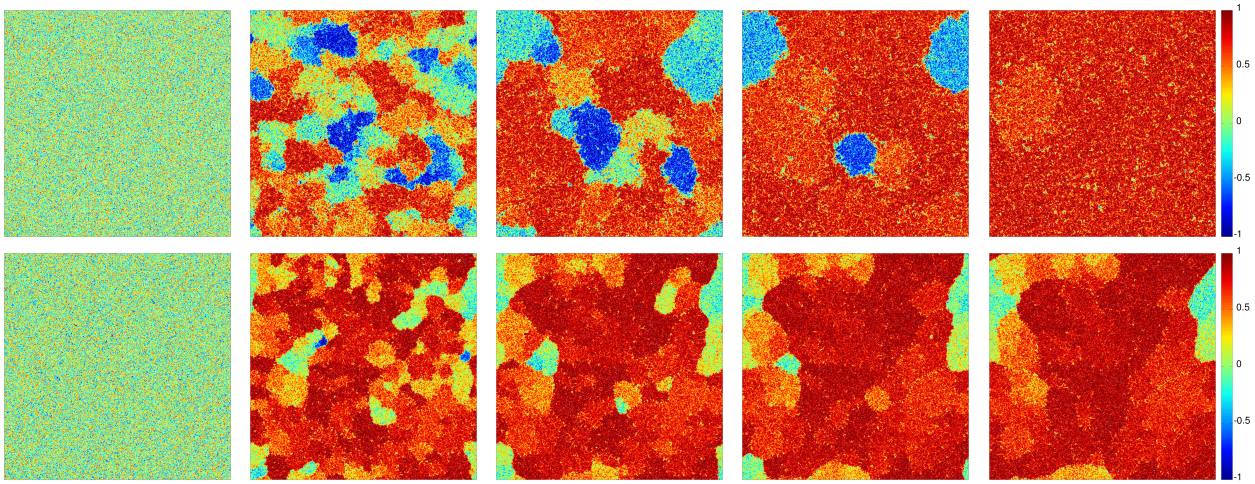

Figure S6. **Evolution of the passive system in the ordered phase**. $\phi = 0.76$ (first row) and $\phi = 0.80$ (second row) at times given in the text.

different: in the first case the asymptotic state is homogeneous and liquid, in the second it is phase separated, and in the last case the configuration is homogeneous with hexatic order, see the correlation data in Fig. S3. We therefore confirm that $\phi = 0.75$ is within the co-existence region of the phase diagram while $\phi = 0.72$ is below its lower limit and $\phi = 0.76$ is beyond its upper limit.

Although we have not discussed the behaviour of the system in the ordered phase in the main text, we show in Fig. S6 two series of the local hexatic order parameter, ψ_{6j}, maps during the evolution of the passive system for densities that are above the boundary of the region of co-existence, $\phi = 0.76$ and $\phi = 0.80$. In both cases the first panels correspond to the initial states and are taken to be random. The subsequent panels show later configurations taken at $4 \times 10^4, 1.8 \times 10^5, 4 \times 10^5, 1.3 \times 10^6$ for both $\phi = 0.76$ and $\phi = 0.80$. After the rather long time elapsed between the next-to-last and last panels in each row, at $\phi = 0.76$ the dynamics reach a stationary homogeneous state while at $\phi = 0.80$, instead, the steady state has not been reached yet and the configuration is polycrystalline, in the sense that large domains with different hexatic order are still present. Indeed, this is the reason why the square data point in Fig. 3 in the main text is away from the curve traced by all other data: longer times are needed to reach the steady state under these high dense conditions. Note, however, that there is no signature of glassiness in the dynamics nor the configuration.

We end in this way the analysis of the passive system.

S3. DYNAMICS IN THE ACTIVE CASE, PE $\neq 0$

In this Section we give additional information on the way in which the activity affects the dynamics and stationary states reached by the interacting dumbbell system. We also illustrate the criteria that we used to delimit the coexistence region in the active case. The plots that we show are complementary to the ones presented in the main text.

Figure S7 studies the effect of a small Pe number and it is an accessory to Fig. 4 in the main text. In the first rows we see two series of local hexatic order grey (colour online) maps taken at different times. The first snapshots in each column are the asymptotic states of the passive system (see Fig. 3 of the main text and Fig. S4) with packing fractions $\phi = 0.74$ (first row) and $\phi = 0.76$ (second row). The former is in the co-existence region of the phase diagram while the latter is in the ordered phase at Pe = 0. In the first case the activity helps accelerate the destruction of the remainder of the horizontal structure and it contributes to build smaller clusters with high hexatic order embedded in a background of low hexatic order. A non-vanishing though rather small Pe has a very strong effect on the second case. It is quite clear from the figures that the ordered state in the first panel is broken in the later panels, and that in the last snapshots regions with higher and lower values of the local hexatic parameter have formed and separated. The system has entered the phase co-existence region under a small amount of activity quantified by Pe = 2.

The discussion in the previous paragraph implies that the upper boundary of the coexistence region moves upwards under increasing Pe. Additional evidence for this claim is given by the panels (b), (c) and (d) in Fig. S7 where the maps of the local density, the modulus of the local hexatic parameter and the probability distribution functions of the latter are shown for $\phi = 0.74$ (above) and $\phi = 0.76$ (below). The probability distribution functions show two peaks. In each case, one of them is incipient, indeed, the one at low $|\psi_{6j}|$ for $\phi = 0.76$ and the one at high $|\psi_{6j}|$ for $\phi = 0.74$. This demonstrates that these cases are close to the upper and lower phase borders in the phase diagram, respectively.

As explained in the main text and in Section S2, a systematic analysis of the appearance and disappearance of the high and low local density peaks and of the local hexatic order parameter allows us to trace the phase boundaries in the phase diagram.

In Fig. S8 we show three subsequent ψ_{6j} maps of a system with packing fraction $\phi = 0.54$ and Pe = 20, that is at the lower limit of densities where phase separation is observed. Starting from a random initial condition, in the course of time, a big cluster with hexatic order grows and it is very clearly seen in the last snapshot in the series. We checked that it maintained roughly this size at later times in the simulation. On the contrary, at smaller packing fractions ($\phi \leq 0.52$) and the same Pe such phase segregation is not observed and the system remains homogeneous at all the running times that we explored.

Figure S9 is an example of a visual way to fix the upper limit of the region of co-existence in the phase diagram. In the upper row we display local hexatic order maps and in the lower row we show the local density. Three Pe numbers Pe = 2, 10, 40 and two packing fractions in each case, one just below and the other one just above the transition line in the phase diagram, are considered. The scales for the density plots are not the same in the various panels to let the different regions in space be identified. It is most clearly seen from the panels with the density plots that below the upper transition line the system is very heterogeneous with regions with distinctly different densities, while above the upper transition line the system is homogeneous.

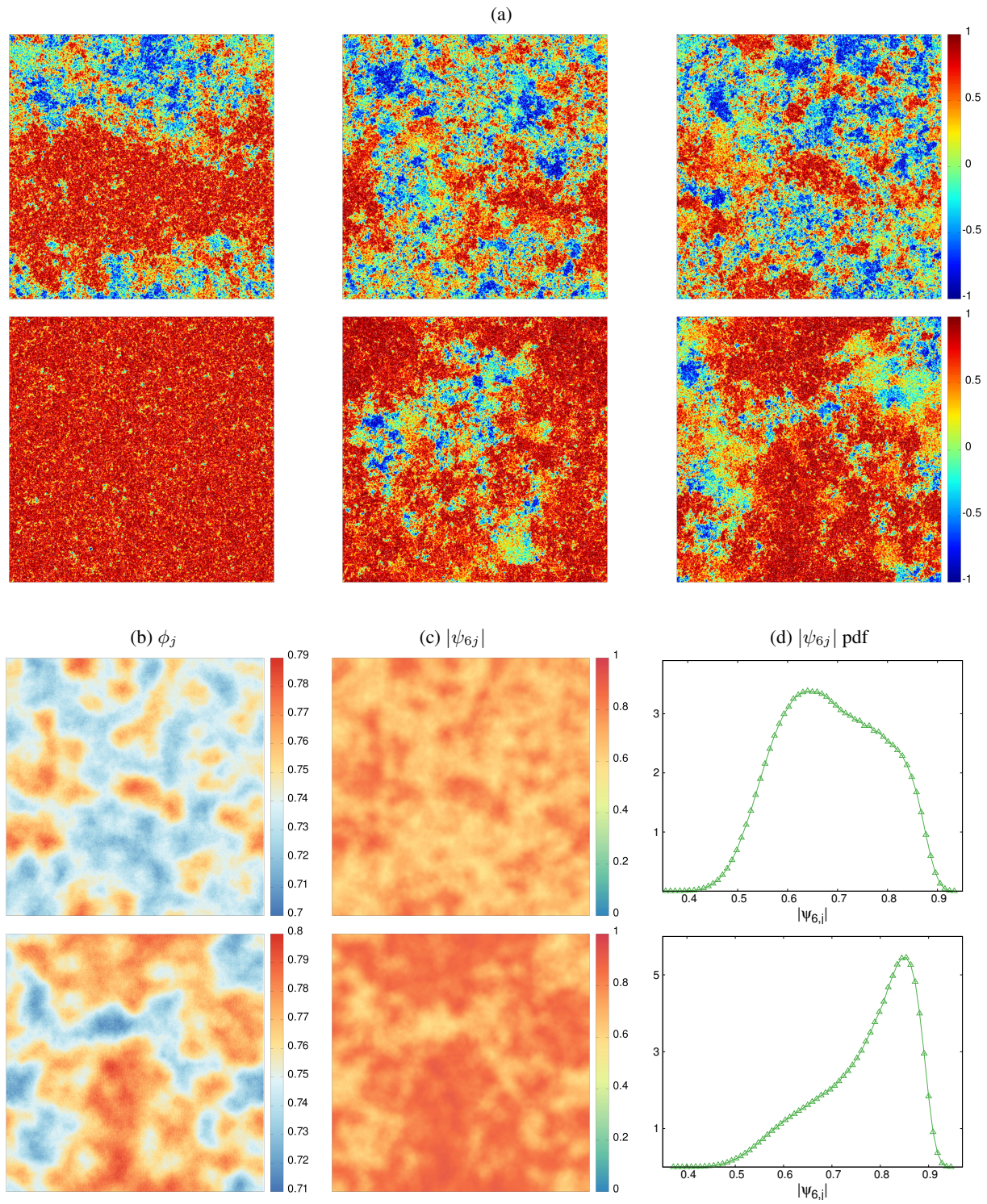

Figure S7. **Effects of activity at small Pe numbers, Pe = 2**. (a) Local hexatic parameter in a system with $\phi = 0.74$ (first line) and $\phi = 0.76$ (second line). The second and third maps were taken after $t = 4 \times 10^4$ and 1.2×10^6 in the first row and $t = 4 \times 10^5$ and 1.2×10^6 in the second row, respectively. In both cases the configurations leading to the last panels are in the stationary regime. (b) Local density contour plot and (c) local modulus of the hexatic parameter of the two stationary configurations in (a). (d) Probability distribution functions of the modulus of the local hexatic parameter at $\phi = 0.74$ (above) and $\phi = 0.76$ (below).

Figure S10 confronts the coarsening dynamics at different Pe numbers and densities. Each column shows data for different Pe ordered from left to right according to Pe = 2, 10, 20, 40. The time arrow runs downwards and the times at which the configurations are analysed are given in the caption. The panels show the different observables that we considered in this study.

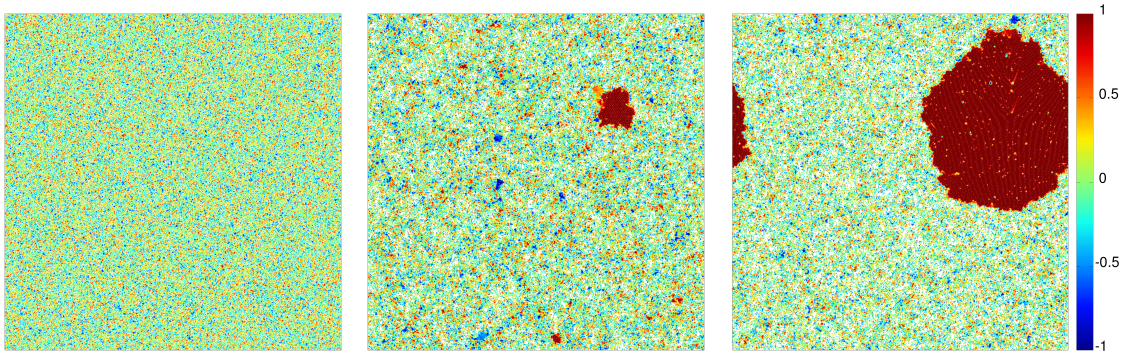

Figure S8. **Determination of coexistence limit at low densities under active forces.** Three local hexatic parameters along the evolution, starting from a disordered configuration, of the active system with Pe = 20, $\phi = 0.54$, at times $t = 0,\ 4 \times 10^4$ and 3.2×10^5. The chosen value of the total surface fraction is the lowest one at which phase separation occurs. The system has been checked to remain homogeneous, just as in the first panel in the row, at $\phi = 0.52$.

We have chosen to show them together to give a complete picture of how the structure is identified from the different graphs. Columns (a) and (b) show the modulus of the local hexatic parameter for Pe = 2 and Pe =10. Column (c) represents the local surface fraction for Pe = 20. Finally, column (d) presents the local hexatic parameter for Pe = 40. All these cases are in the region of the phase diagram with phase separation. We signal here the presence of light lines within dark regions in the configuration at the longest time in column (b): they are domain boundaries between clusters with different local hexatic order parameter that in the representation in which the modulus of ψ_{6j} is shown look the same.

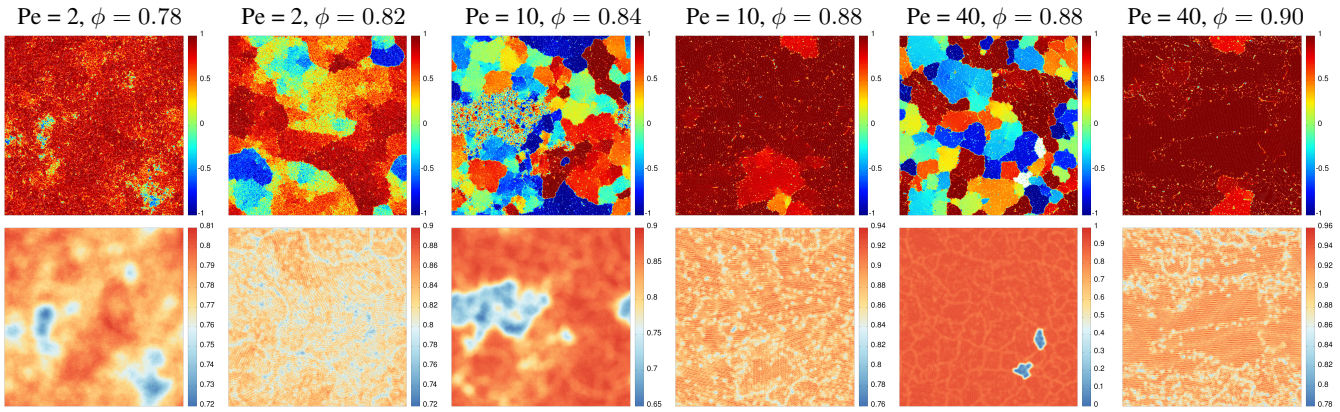

Figure S9. **Determination of the co-existence upper limit under active forces.** In the upper row the local hexatic parameter and in the lower row the local density profile. The parameters are written in the upper line in the figure. For each Pe number we compare the stationary state at two different packing fractions just below the limit of co-existence and just above it. Note that colour code is not the same on the various panels.

We close with four films that exhibit the coarsening dynamics of the active system in the region of the phase diagram with phase co-existence. The movies present the map of the absolute value of the local hexatic parameter. The ordered region has uniform color and a value of $|\psi_{6j}|$ around 1, which can be clearly distinguished from the disordered one.

Movie M1 shows the dynamics of a system with $\phi = 0.74$ and Pe = 10 starting from a configuration that has evolved at Pe = 0 from an ordered central stripe. The introduction of activity quickly destroys this order and is followed by the formation of more compact clusters. The movie includes at second 16 a zoom over a restricted region where one can appreciate a dense zone with almost perfect orientational order surrounded by a low-density and quite disordered spatial region. The phase separation is most clearly seen in this representation. Of course, neither the dense nor the loose regions are static and the film clearly shows how the former breaks and reforms with different shape in the course of time.

The other three movies, M2-M4, are taken at parameters in the ϕ-Pe phase diagram that reproduce roughly a disordered and

ordered phase occupying the same area. In order, M2 is at $\phi = 0.756$ and Pe = 2, M3 at $\phi = 0.78$ and Pe = 10, M4 at $\phi = 0.734$ and Pe = 20. In particular, M2 starts from a random configuration, while M3-M4 are initiated at an equilibrated configuration at Pe = 0.

Finally, we insist here upon a fact already mentioned in the description of Fig. S10 (b). In the three cases in which Pe = 10 or 20 (movies M1, M3, M4), it can be clearly seen that the domains with dark colour (large value of the modulus of the local hexatic parameter) are threaded by lines of light colour (low value of the local hexatic parameter). These lines correspond to domain walls between regions with different orientational order.

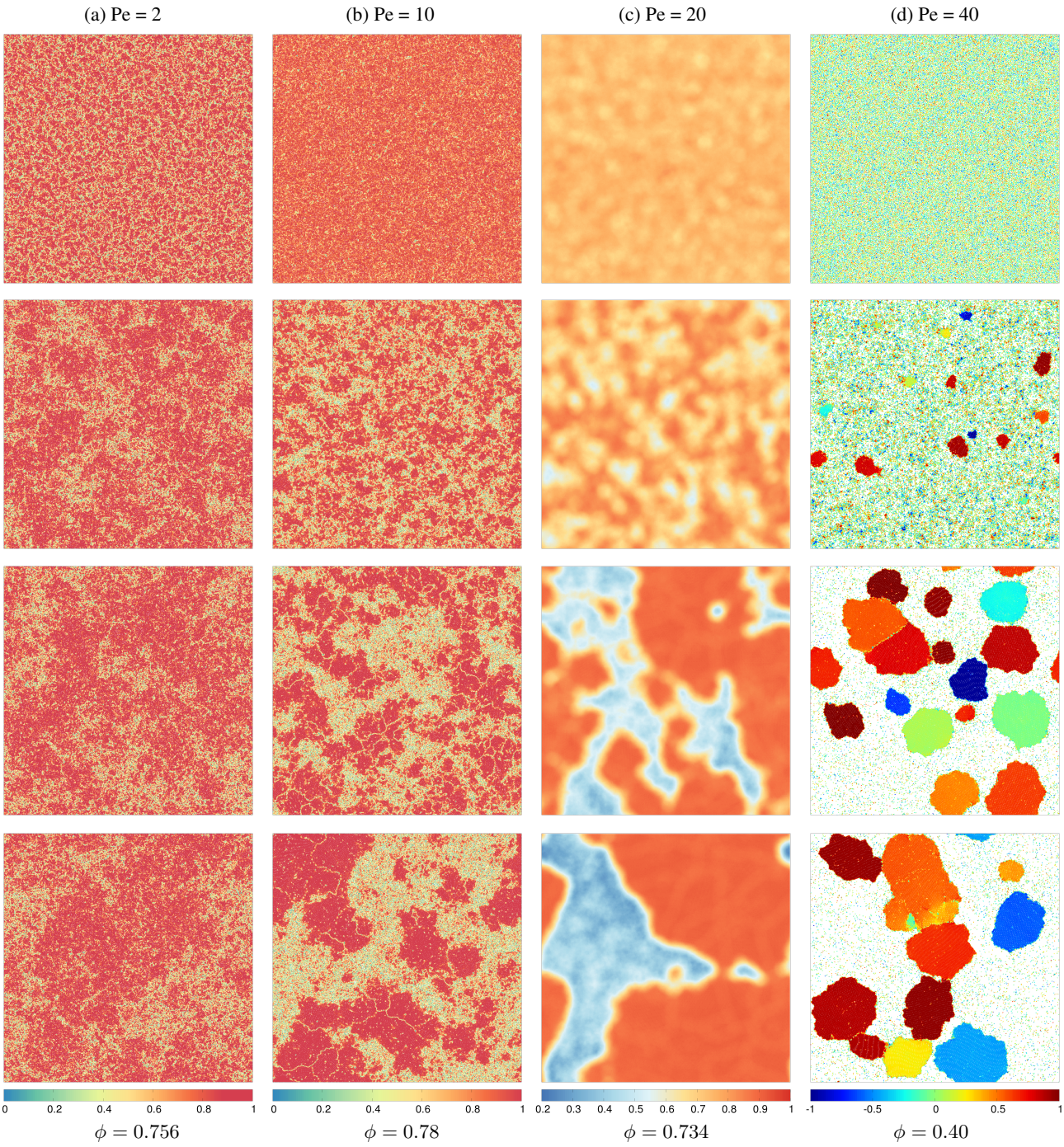

Figure S10. **Examples of coarsening at different Pe numbers** Four snapshots of the evolution, starting from a disordered configuration, for the active system with (a) Pe = 2, $\phi = 0.756$, $t = 8 \times 10^2,\ 3.2 \times 10^5,\ 8 \times 10^4,\ 1.8 \times 10^5$; (b) Pe = 10, $\phi = 0.78$, $t = 0,\ 4 \times 10^1,\ 8 \times 10^3,\ 2.2 \times 10^5$; (c) Pe = 20, $\phi = 0.734$, $t = 0,\ 1 \times 10^3,\ 2 \times 10^4,\ 1.1 \times 10^5$; (d) Pe = 40, $\phi = 0.40$, $t = 0,\ 2 \times 10^3,\ 4 \times 10^4,\ 1.5 \times 10^5$. Time runs vertically from top to bottom. For each Pe, the chosen values of the total surface fraction is the lower one at which the active system phase separates. For Pe = 10 the first snapshot is similar to the one observed at $\phi = 0.68$. For Pe = 20 the system has been checked to remain homogeneous at $\phi = 0.52$. (a) Modulus of the local hexatic parameter, (b) the same, (c) local surface fraction, (d) local hexatic parameter.